Applied Organometallic Chemistry

WILEY

Applied Organometallic Chemistry

RESEARCH ARTICLE OPEN ACCESS

Formic Acid Dehydrogenation Catalysis Using Novel Pyridyl-Formamidine Half-Sandwich Ruthenium(II) Complexes

Juliana Mana Edor[1] | M. Cassiem Joseph[2] | Johan H. L. Jordaan[1] | Hermanus C. M. Vosloo[1] | Andrew J. Swarts[2]

[1]Catalysis and Synthesis Research Group, Research Focus Area for Chemical Resource Beneficiation, North-West University, Potchefstroom, South Africa | [2]Molecular Sciences Institute, School of Chemistry, University of the Witwatersrand, Johannesburg, South Africa

Correspondence: Andrew J. Swarts (andrew.swarts@wits.ac.za)

Received: 14 October 2024 | **Revised:** 11 December 2024 | **Accepted:** 17 January 2025

Funding: This work was supported by the National Research Foundation (127291 and 137758), Styrelsen för Internationellt Utvecklingssamarbete, Schlumberger Foundation and the Organization for Women in Science for the Developing World.

Keywords: dehydrogenation | formic acid | homogeneous catalysis | hydrogen | ruthenium hydride

ABSTRACT

The reaction of N,N′-bidentate chelating ligands with $[Ru(p\text{-cymene})Cl_2]_2$ in methanol resulted in six-membered Ru complexes with tshe general formula [RuCl(*p*-cymene)**L**]Cl exhibiting a pseudo-octahedral piano-stool geometry. The combination of NMR, MS, FTIR and SCXRD techniques confirmed the successful synthesis of the reported compounds. The prepared complexes were all active in formic acid dehydrogenation (FADH) catalysis, producing an equimolar mixture of H_2 and CO_2 gases with no detectable amount of CO. Establishing thermodynamic and kinetic parameters provided evidence for the role of pre-catalyst and FA during catalysis. Reactivity studies between **C6** and HCOOK revealed complex equilibria and allowed for the detection of the key monohydride species involved in catalysis. Remarkably, **C6** proved to be robust at 100°C, resulting in approximately 98% substrate conversion with a total TON of about 7892 and TOF close to 300 h^{-1} after 35 h.

1 | Introduction

Ruthenium belongs to the platinum-group metals (PGMs), and its compounds are often considered one of the most active catalysts for several reactions of commercial and environmental importance [1]. It is unique and multifaceted due to its ability to assume a variety of coordination modes and exhibits a wide range of oxidation states from 0 to 6 in its compounds [1]. However, Ru catalysts have essentially been synthesised in the +2 oxidation state, as they have proven efficient in many catalytic reactions such as hydrogenation [2, 3], oxidation [4, 5], metathesis [6–8], polymerisation [9] and double-bond functionalisation [9]. Various ligands have been successfully complexed to Ru metal, including Schiff base ligands [10], carboxylates [11], triazoles [1, 3, 12], carbenes [1] and amidinates [13]. Among the PGMs, Ru is usually considered the metal of choice in catalysis because its compounds are relatively less expensive than the other PGMs (Pd, Pt, Rh and Ir) [14]. The past few decades have witnessed a surge in the development of Ru complexes with both achiral and chiral configurations for potential applications in various fields [15]. In terms of 'half-sandwich' organometallic compounds, they typically contain a metal centre with four different ligands, where one of the ligands is a cyclic polyhapto hydrocarbon, which is facially bound to the metal centre [15]. Ruthenium complexes with the half-sandwich motif have been studied because of their ease of functionalisation, broad catalytic activities and stability. Furthermore, Ru compounds have received much attention as potential anticancer agents. Therefore, the chemistry of the ruthenium compounds is very diverse [15], and it is important to expand the scope of its compounds through ligand development.

Growing worries about the environment due to using fossil fuels necessitate exploring eco-friendly alternatives such as green fuels. One such option is FA, which can be obtained by hydrogenating CO_2. Recently, FA has gained considerable attention as a liquid hydrogen storage material due to its stability, low toxicity, low flammability, biodegradability at normal conditions and comparatively high H_2 content. Compared with other H_2 storage materials, FA decomposition has a low-reaction enthalpy, which means that H_2 can be produced from FA at relatively low temperatures. Furthermore, FA dehydrogenation is thermodynamically advantageous, making producing high-pressure H_2 from FA easier than other H_2 storage chemicals [16]. Additionally, FA can be used as a renewable source for hydrogen storage. CO_2, a by-product of FA decomposition, can be reduced back to FA using the appropriate catalysts, thereby making the process sustainable. Numerous noble metal catalysts have been investigated for the selective breakdown of FA to produce H_2 with high efficiency [17]. It is worth noting that Ru-based catalyst systems have gained considerable attention due to their affordability in comparison with the other platinum group metals [14], coupled with their efficiency in formic acid dehydrogenation (FADH) catalysis.

We have recently reported the one-pot method for the preparation of new pyridyl-formamidine ligands and their coordination behaviour in the presence of precious and non-precious metals [18]. We found that bidentate N,N′ chelation was the favoured mode of coordination, forming six-membered chelates in the case of Mn(I), Cu(II) and Pd(II). Using acetate salts of Cu(II) and Zn(II), we found that base-mediated (likely acetate) hydrolysis occurred on the formamidine functionality, necessitating careful choice of metal precursor during complexation. As a further development of the utility of our pyridyl-formamidine ligands as a viable scaffold, we present the application of novel pyridyl-formamidine–ligated half-sandwich ruthenium complexes as catalysts in the dehydrogenation of formic acid (FA), providing a comprehensive report of their synthesis, catalytic optimisation and mechanistic elucidation.

2 | Results and Discussion

2.1 | Synthesis and Characterisation of Complexes (C1–C8)

The complexes were synthesised by reacting dichloro(*p*-cymene)ruthenium(II) dimer with our previously reported pyridyl-formamidine ligands [18] in methanol at room temperature overnight to obtain the desired complexes (Scheme 1). After the allotted time, the solvent was reduced, and the product precipitated with diethyl ether or hexane to afford the orange powder product. All the complexes were characterised by a combination of FTIR, ^{1}H and ^{13}C {^{1}H} NMR spectroscopy, ESI-MS, elemental analysis and SCXRD.

The FTIR data provided evidence for the coordination of the ligands to the Ru centre. Weak absorption bands around 3300 cm^{-1}, corresponding to the N–H stretching vibration of the secondary amine, were observed, similar to those seen in the ligands. However, notable redshifts were detected in the stretching frequencies of the imine and pyridinyl imine moieties in the ligands and their corresponding complexes. Specifically, the $\nu(C{=}N)_{imine}$ shifted from approximately 1650–1675 cm^{-1} in the ligands to a lower range of 1629–1648 cm^{-1} in the complexes. Similarly, the $\nu(C{=}N)_{py}$ shifted from about 1555–1578 cm^{-1} in the ligands to 1523–1542 cm^{-1} in the complexes. These shifts are likely due to the electron-withdrawing effects of the coordinated metal, which weakens the C=N bond and thus lowers the stretching frequency [4].

The ^{1}H NMR spectra of the pyridyl-formamidine complexes show significant downfield shifts for the secondary amine protons from 8.89–10.41 ppm in the ligands to 13.19–13.57 ppm in the complexes. The imine protons also showed appreciable shifts from the free ligands to the complexes. The shift in the signals indicates the successful coordination of the ligands to the ruthenium metal through the displacement of a chloride, which then serves as a counter-ion. Additionally, the ^{1}H NMR spectra of all the complexes suggest a loss of the two-fold symmetry of the *p*-cymene upon coordination of the metal to the pyridyl-formamidine ligands [4, 19]. Thus the *p*-cymene proton signals appear as four distinct doublet peaks with chemical shifts ranging between 4.56 and 5.70 ppm (Figure S1). The ^{13}C NMR spectra also show a significant downfield shift for the signals of the imine carbon. For instance, in complex **C1**, there is a downfield shift from 149.4 ppm in the ligand to 155.7 ppm in the complex (Figure S3). This trend is seen in all the complexes, and these results further support the successful coordination of the ligands to the metal.

High-resolution ESI-MS analysis, conducted in the positive mode, consistently matched the suggested ruthenium structures. Within a typical spectrum, the base peak is observed together with additional fragments. The base peak displays a characteristic isotopic pattern corresponding to the cationic fragment of complexes as illustrated in Figure S4, in agreement with the calculated isotopic pattern. Additional characterisation through elemental analysis validates the bulk purity of these cationic ruthenium complexes, with the experimental elemental data closely matching the calculated values. These findings suggest that the ruthenium complexes are synthesised in a metal-to-ligand ratio of 1:1.

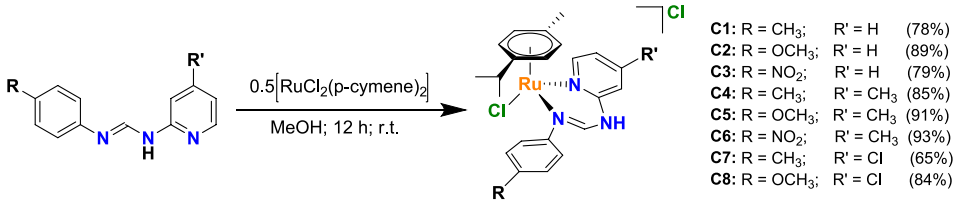

SCHEME 1 | Synthetic routes to ruthenium pyridyl-formamidine complexes.

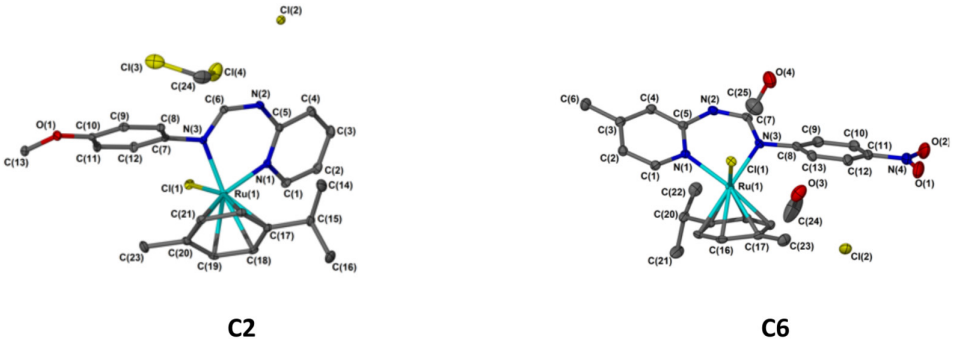

FIGURE 1 | The molecular structures of **C2** and **C6** with thermal ellipsoids drawn at 30% probability level. Hydrogen atoms have been omitted for clarity.

TABLE 1 | Screening of compounds **C1**–**C8** in FADH[a].

Entry	Compound	TON at 3 min	TOF (h^{-1})	Conversion%
1	**C1**	6.1	123	> 99
2	**C2**	4.1	82	> 99
3	**C3**	6.1	123	> 99
4	**C4**	8.2	164	> 99
5	**C5**	4.1	82	> 99
6	**C6**	16.4	327	> 99
7	**C7**	6.1	123	> 99
8	**C8**	14.3	286	> 99

[a]Conditions: The results are the average of two readings each, with an error margin < 5%. The TONs and TOFs were calculated based on the total volume of gas produced in the first 15 min. The conversions were determined when the reaction stopped, and no more gas was generated. Catalyst: 0.05 mmol. FA: 5 mmol. HCOONa: 1 mmol. Temperature: 80°C. Solvent: DMF.

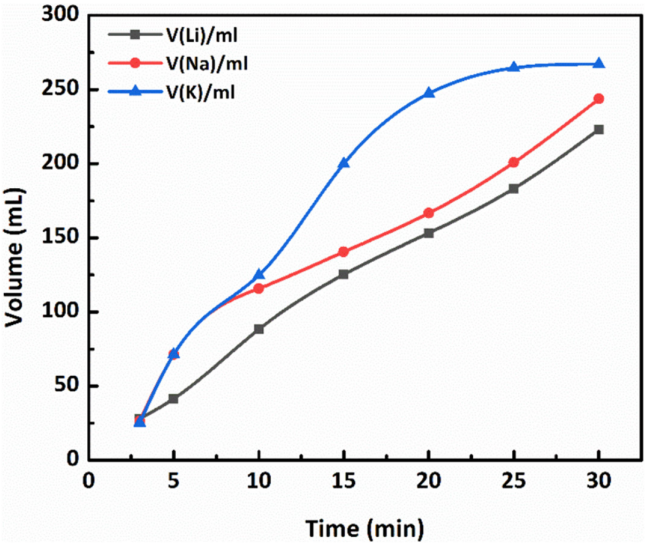

FIGURE 2 | Influence of the nature of the formate cation on the activity of the catalyst. Reaction conditions: catalyst = 0.05 mmol, HCOOM = 1 mmol, temperature = 80°C, FA = 5 mmol, DMF = 1 mL.

2.2 | Synthesis and Characterisation of Complexes (C1–C8)

The molecular structures were determined using single-crystal X-ray diffraction. Single crystals suitable for X-ray analysis of complexes were obtained through the slow evaporation of a solution of the complex in a mixture of dichloromethane and diethyl ether at room temperature. Figure 1 shows the molecular structures of compounds **C2** and **C6**, while the remaining structures are provided in Figure S5. The complexes have the [(*p*-cymene)RuCl(**L**)]$^+$ cationic species and the Cl^- counteranion. In all the complexes, the Ru centre is bonded to the N,N′-bidentate pyridyl-formamidine ligand through the N atoms of the imine and the pyridine ring, the *p*-cymene arene ring and a terminal chloride to form a pseudo-octahedral 'piano-stool' geometry. The chloride atom is seen on the opposite side of the isopropyl group of the *p*-cymene, similar to related compounds previously reported [4, 18]. The Ru–N bond lengths in the complexes range between 2.093 and 2.114 Å, which is consistent with Ru *p*-cymene/arene compounds reported previously [5, 19, 20]. Additionally, the observed N–Ru–N′ angles range from 84.94° to 87.37°, which are much smaller than the ideal geometrical value but comparable to Ru *p*-cymene/arene compounds with N,N′ donor ligands [21, 22]. The deviation from the ideal value is attributable to the geometric backbone constraint of the chelating ligands, which is known to influence the size of the bite angles of transition metal complexes [23, 24].

2.3 | Use of C1–C8 in FADH Catalysis

Following the procedure outlined in Section 4.3, the dehydrogenation of FA was investigated with the different pyridyl-formamidine ruthenium complexes (**C1**–**C8**) in DMF at 80°C using an alkali metal formate additive (HCOONa) in a 1:5 M ratio to FA. Complexes **C1**–**C8** were all found to be active in the dehydrogenation of FA, reaching the maximum conversion of the substrate in less than 1 h. Comparing the activity of compounds **C1**–**C8**, it was observed that the complexes with methyl substituents on the pyridine ring performed slightly better than the unsubstituted and chloro-substituted analogues. This is attributable to a more electron-rich metal centre leading to higher catalytic activity. Reek et al. found a correlation between the electronic property and activity of the sulphonamide organic side group using an Ir catalyst with a phosphine-functionalised sulphonamide ligand, where high activity was obtained with an electron-donating group in the para position, whereas an

electron-withdrawing group in the para position results in much lower activity [25]. Table 1 shows the various TON and TOF values recorded. Complex **C6** was the best-performing and was used to optimise the reaction conditions (Entry 6). The gas mixture was analysed with GC-TCD, and the results indicated the presence of only H_2 and CO_2 in a 1:1 ratio (Figure S2). No CO was detected, indicating that FADH proceeds selectively over dehydration.

2.3.1 | Influence of the Alkali Metal Formate Additive

Other alkali metal formate additives, namely, Li and K formates, were also screened, and the results were compared with those generated using HCOONa. No reactivity was observed in the absence of an alkali metal formate. A plot of the volume of gas generated with time within the first 30 min of the reaction was used to determine the best-performing formate additive (Figure 2). Interestingly, under the same reaction conditions, HCOOK performed slightly better than HCOONa and HCOOLi, respectively. This shows that the role of the formate is not necessarily due to its Lewis acidity, in agreement with the observation made by Huang et al. [26], when a ruthenium complex bearing an N,N′-diimine ligand was employed in FADH [25]. The observed trend of K > Na > Li in this study could be due to the relative ease with which HCOOK reacts with the precatalyst to generate the hydride species. Due to its larger size, K has a greater tendency to react with Cl than Na and Li, according to the HSAB principle [27]. However, Albrecht et al. reported that the alkali cation of the formate additive has a distinctly promotional effect on the catalytic activity along the series Li > Na > K using a low-coordinate iridium complex [28]. They rationalised their observation on the Lewis acid activation of the FA substrate, which is in good agreement with another report where iron complexes were used in FADH [29].

The amount of formate additive used also influences the reaction rate and the total volume of gas generated. It was observed that when 1 mmol of the formate additive was used (i.e., a 1:5 ratio of formate additive to FA, respectively), the total volume of gas generated exceeded the amount of gas expected to be produced. Upon further investigation, where only the formate additive was used without the substrate, it was observed that the catalyst can dehydrogenate HCOOM to produce a 1:2 mixture of H_2 and CO_2, respectively. Based on the above investigation, it is important to use stoichiometric amounts of the formate additive with respect to the precatalyst, thereby limiting the excess gas produced due to the presence of excess amounts of formate additive in the system. The amount of formate additive was therefore varied, using 1:1, 1:1.5 and 1:2 precatalyst-to-formate ratios, respectively (Table S3). The maximum theoretical volume of gas expected if all the FA (5 mmol) is converted is ~260 mL. A 95% (~237 mL) conversion was observed when a 1:1 ratio was used, but when 1:1.5 was used, > 99% (~265 mL) conversion was achieved, and > 100% (~270 mL) conversion was achieved with a 1:2 ratio. The excess gas (~10 mL) observed with the 1:2 ratio did not necessarily correspond to the calculated excess amount of formate that should be present after activation of the catalyst. It was found that the value was slightly lower than expected, and this could be due to slight variations in measurement, expected when using the volume displacement method.

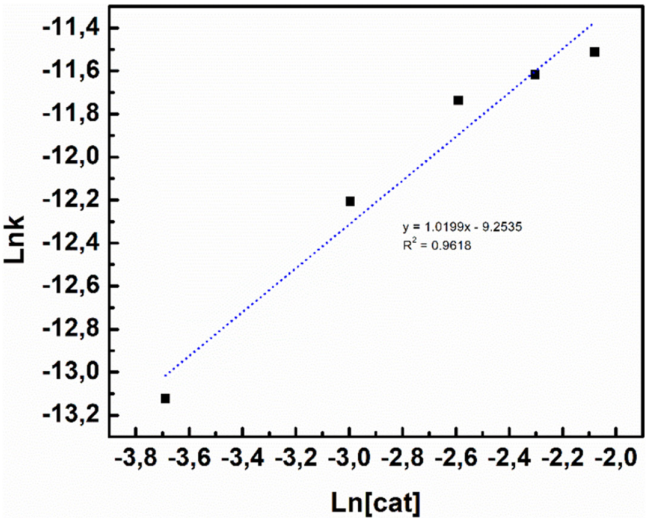

FIGURE 3 | Rate order determination from the plot of ln[k] vs. ln[**C6**] from the rates deduced from concentration-dependent catalysis.

2.3.2 | Influence of the Reaction Temperature

A range of reaction temperatures from 60°C to 100°C were investigated. No evolution of gas was observed at room temperature. A plot of conversion against time at various temperatures is illustrated in Figure S6. The initial reaction rate increased by increasing the temperature with a TOF of about 692 h^{-1} recorded in the first 5 min at 100°C, while at 90°C, 80°C and 60°C, the TOFs recorded were 327, 274 and 30 h^{-1}, respectively. The reaction rate was significantly slower at 60°C, with maximum substrate conversion achieved after approximately 180 min (3 h). When the temperature was increased to 80°C under the same conditions, the maximum conversion was attained in approximately 60 min, and at 100°C, the maximum conversion was achieved in about 30 min. The curves are sigmoidal and show an induction period (~10 min) at lower temperatures. The increase in the rate of FADH with increasing temperature has been reported with various catalyst systems, including Ru-based catalysts [30–32]. The observed trend could be attributed to the increased kinetic energy of the system at high temperatures, which augments the collision frequency, thereby increasing the rate of the reaction [33]. To determine the thermodynamic activation parameters, Arrhenius and Eyring plots (Figures S6b and S6c, respectively) were constructed. The activation energy (E_a) calculated from the slope of the Arrhenius plot is 61 kJ mol^{-1}. Similarly, an Eyring plot of the rates at different temperatures resulted in $\Delta H^{\ddagger} = 64$ kJ mol^{-1} and $\Delta S^{\ddagger} = -71$ J K^{-1} mol^{-1}. The entropy value points to a transition state with associative character [28]. These values are comparable to those reported in FADH reactions catalysed by noble metals [34].

2.3.3 | Influence of the Precatalyst Concentration on the Reaction Rate

The dependence of the catalyst concentration on the rate of FADH was investigated by using the initial rates obtained when the concentration of **C6** was varied, ranging from 0.025 to 0.125 mol L^{-1} at 100°C with 5 mol L^{-1} of FA in 1 mL DMF (Figure S7). Plotting the

rate of gas production versus the catalyst concentration resulted in a linear correlation as illustrated in Figure 3. This provides evidence for a first-order rate dependence on the concentration of complex **C6**, consistent with a mononuclear active species in the rate-determining step. Under these conditions, no saturation behaviour was observed as evidenced by the absence of a plateau in the rate; however, this may occur at higher catalyst concentrations. Next, the influence of the concentration of FA on the rate was investigated (Figure S8). The order of the reaction as determined from the plot of ln[k] vs. ln[FA] in Figure 4 points to an approximate half-order dependence on [FA] concentration. This observation provides evidence for a pre-equilibrium existing between FA/formate and the Ru centre to generate Ru-formate during the activation step, while supporting a hydrogen production pathway that does not involve FA–mediated protonation [32].

2.3.4 | Influence of the Solvent

The dehydrogenation of FA was performed in various organic solvents utilising **C6**, which were selected based on considerations from literature reports and considering their boiling points and availability. The solvents assessed included DMF, DMSO, chlorobenzene, and toluene, as detailed in Table S4. The findings indicated DMF's superiority over DMSO, chlorobenzene and toluene. Notably, when DMSO was employed, complete conversion was attained in 90 min, whereas the use of DMF led to an accelerated reaction rate, achieving total conversion in approximately 20 min under optimal conditions. This may be attributed to the basic properties of DMF, providing a buffering effect during catalysis and preventing the deactivation of the active species [35]. In contrast, chlorobenzene and toluene exhibited significantly lower activity, yielding only 27% and 22% conversion, respectively, after 120 min. The catalyst's reduced activity in toluene could be attributed to its low solubility in toluene, even at elevated temperatures. However, in the case of chlorobenzene, despite the catalyst's solubility at room temperature, its poor performance could not be solely attributed to solubility issues. Considering the superior performance of DMF and DMSO, it is conceivable that using strongly coordinating solvents plays a role in stabilising a key intermediate species, thereby enhancing the system's activity [36]. Unfortunately, our system exhibited poor performance under neat conditions, despite the catalyst's high solubility in FA. This observation suggests that the catalyst may undergo deactivation in highly acidic conditions, possibly due to the irreversible formation of off-cycle intermediates catalytically inactive species such as dimers or trimers [37], or that FA condenses into the reactor's headspace, becoming inaccessible to the catalyst [30]. To further probe the stability of the complexes in various solvents, NMR studies were conducted in DMSO-d_6, CD_3CN, $CDCl_3$ and $CDCl_3$/DMF mixtures over 2 months. In all solvents, including the $CDCl_3$/DMF mixture, no significant changes were observed in the ^1H NMR spectra after an aging period of 2 months (Figures S9–S12). The result highlights the solution stability of **C6**, an important consideration when designing industrially relevant pre-catalysts. We further assessed the solution stability of **C6** at elevated temperatures of 90°C over a period of 120 h in DMSO-d_6 with NMR spectroscopy (Figure S13). Within 24 h, characteristic signals corresponding to coordinated *p*-cymene disappeared, accompanied by the appearance of signals assigned to free *p*-cymene. While **C6** is thermally unstable under non-catalytic conditions, it shows markedly higher stability under catalytic conditions (either stepwise or continuous FA addition) as described in Sections 2.3.5 and 2.3.6.

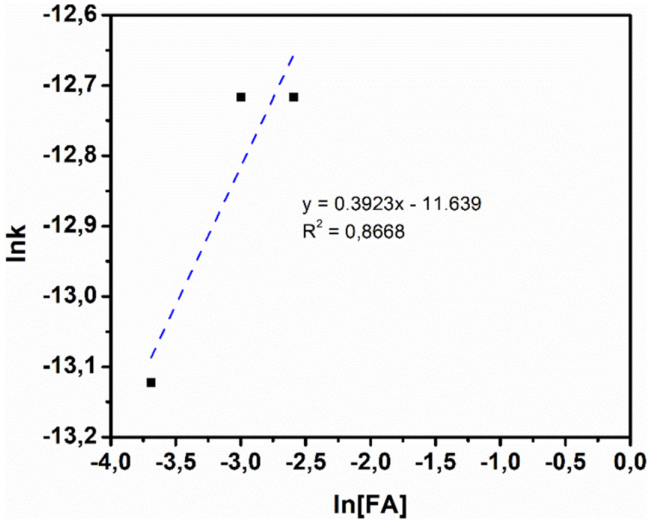

FIGURE 4 | Rate order determination from the plot of ln[k] vs. ln[FA] from the rates deduced from concentration-dependent studies.

2.3.5 | Recyclability of C6 in FADH

To determine the robustness of the precatalyst under the optimum reaction conditions, 5 mmol (0.2 mL) of FA was added by manual injection via a septum into the reactor every 20 min (the time when almost all the FA is converted) up to 12 cycles, as illustrated in Figure S14. A total conversion of approximately 98% was recorded, resulting in a total TON of 1176 and TOF close to 300 h^{-1} after the 12 cycles. This demonstrates the robustness of the system even at high temperatures. Under these conditions, it is worth noting that the resultant formate-to-substrate ratio could be considered negligible. The wavy nature of the plot is an indication of the pH dependence of the system, which is consistent with other reported systems that demonstrate pH dependence [27]. Therefore, it is conceivable that when FA is freshly introduced into the system, the rate is lowest due to the increased acidity of the system, but as the FA is consumed, the system becomes less acidic, and the rate increases as the reaction proceeds. This indicates that the catalyst works better at higher pH values. Therefore, this provides additional evidence supporting the earlier observations made where higher FA concentrations resulted in lower reaction rates.

2.3.6 | Continuous FA Addition With C6

To determine the longevity of the system under the optimised reaction conditions, FA was continuously added via an automatic syringe pump at a constant rate. Under these conditions, a steady gas flow rate of about 550 mL h^{-1} was recorded for over 35 h. Figure S15 illustrates the time course of gas evolution during the continuous FA addition. The catalytic activity was not significantly hindered by the long reaction time or the temperature (100°C). This further demonstrated the robustness of the system. A total TON of about 7892 and TOF of 225 h^{-1} was recorded after 35 h of reaction.

2.3.7 | Establishing the Reactivity of C6 With HCOOK

We sought to elucidate the mechanistic features of our catalyst system utilising **C6** (Scheme 2). To this end, a yellow solution of **C6** was reacted with 1 equivalent of HCOOK in DMSO-d_6 to afford a red-orange solution (Figures S16 and S17). The disappearance of the N*H* proton of the ligand backbone is noted upon the addition of HCOOK, which forms **C6′** via formate-mediated deprotonation, based on literature precedent (Scheme 2) [26]. This highlights the non-innocence of the pyridyl-formamidine ligand in formate-promoted FADH. No hydride formation was observed under these conditions, even after prolonged reaction time of 16 h (Figure S16). The reaction was repeated in the presence of 10 equivalents of HCOOK, affording identical colour changes. It should be noted that this reaction shows the evolution of several major and minor hydride species over a 22-h period, which are indicative of complex dynamic equilibria, specifically under non-catalytic conditions (Figure S17). A first major hydride signal is observed at δ −7.5 ppm, assigned to species **C6a**, a Ru(II)-formato complex, formed under basic conditions, in analogous fashion as observed for Ru-Zn polymetallic complexes, reported as hydrogenation catalysts [38a]. After 10 min, a second major hydride signal has evolved at δ −14.5 ppm, assigned to species **C6b**, a Ru(II)-(η^2-CO_2)hydride, which is related to the hydride complex, [Ru(tppts)$_2$H(η^2-CO_2)(H_2O)$_2$] [38b]. Species **C6b** increases in intensity over the next 50 min, with a concomitant decrease in intensity for **C6a**. These two species are presumed to be in equilibrium, initially shifted to **C6a**, in line with stronger coordination of formate than carbon dioxide as ligand [39]. After 90 min of reaction, species **C6a** has been converted into **C6b** (minor) and a new major hydride species, **C6c**, the Ru(II)-monohydride. Species **C6c** is presumed to be protonated under catalytic conditions, forming **C6-hydride** (Scheme 2) [26]. This protonation step is not observed under our experimental conditions, which were designed to probe the role of N-H and its potential non-innocence during hydride generation. The completion of the catalytic cycle proceeds via two potential pathways as illustrated in Scheme 3. Pathway a) proceeds with the involvement of FA in the dihydrogen formation step through the protonation of **C6-hydride** and would proceed with

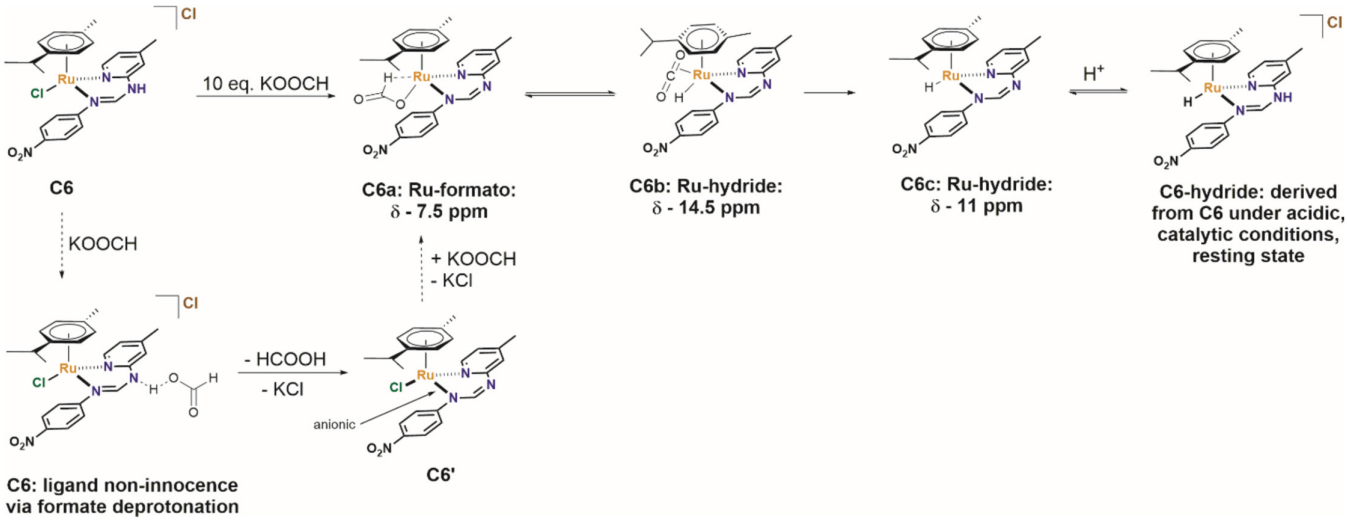

SCHEME 2 | Formate-mediated Ru-hydride (**C6c** and **C6-hydride**) formation with **C6**.

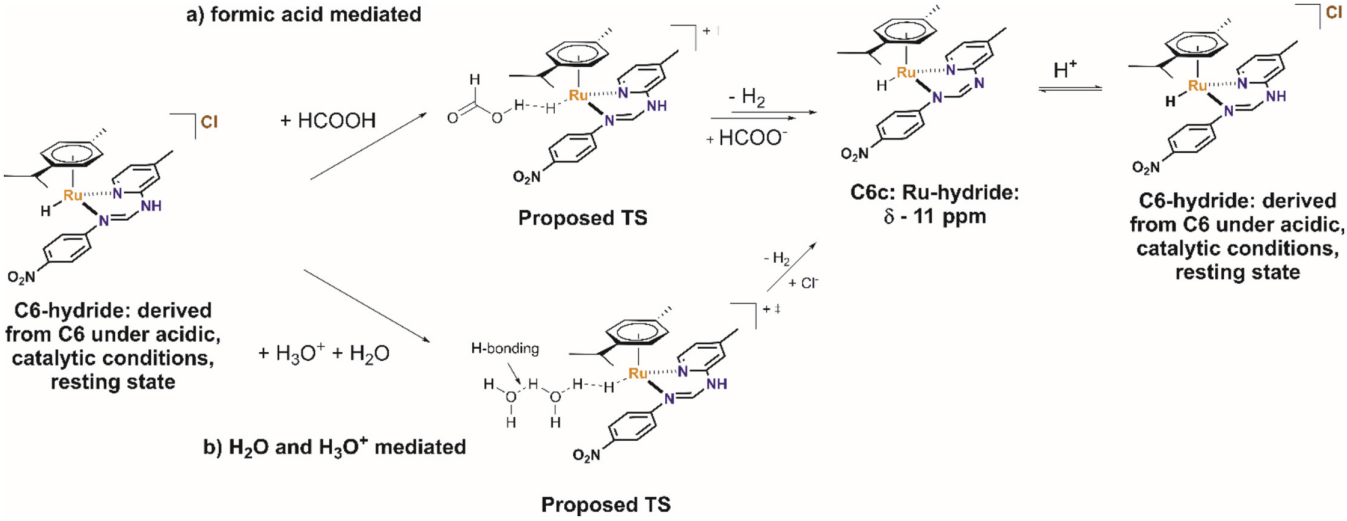

SCHEME 3 | Hydrogen production pathways from **C6-hydride**.

first-order dependence on [FA]. Pathway b) proceeds with the involvement of hydronium ions protonating **C6-hydride** to form dihydrogen. The half-order in [FA] observed for our catalyst system provides evidence for the involvement of hydrated protons as the hydrogen source, in analogous fashion to other reported Ru(II) catalyst systems [26].

2.3.8 | Comparative Analysis With Reported Systems

Table S5 presents data related to a comparative analysis between selected catalyst systems and those outlined in the present study, focusing on isolated reactions under optimised conditions. The first few entries showcase the state of the art in dehydrogenation catalysis. Specifically, Entry 1 showcases a water-soluble Ir complex, **I**, capable of dehydrogenating FA with TON 2.4 million at 80°C, in the absence of additive [32]. Albrecht's group reported the current state of the art in Ir-catalysed FADH (Table S5, Entry 2). Utilising an Ir-catalyst bearing a phenoxy-PYE ligand, **II**, FA could be dehydrogenated in the presence of lithium formate (1 equivalent) with TONs of 2 million and steady-state TOF of 80,000. A cost analysis shows the viability of the system under industrially relevant conditions, despite requiring a substantial amount of additive [28]. Milstein reported a PNP-ligated Ru-hydride, **III**, which dehydrogenated FA with TONs of 1.7 million and TOF of 3100 under neat conditions (Table S5, Entry 3) [30]. Filonenko et al. reported the dehydrogenation of FA with a (PNP)Ru-hydride complex, **IV**, with triethylamine as an additive. A maximum TOF of 257,000 h^{-1} and TON of 326,500 was obtained at 90°C in DMF solvent (Table S5, Entry 4) [36]. Our catalyst system with **C6** outperforms several reported systems derived from Ru and other metals. The π-coordinated phenoxy-ligated Ru-dimer, **V**, reported by Verron et al. was found to dehydrogenate FA with a TON of 173 and $TOF_{initial}$ of 202 h^{-1} in DMSO at 90°C (Table S5, Entry 5) [40]. The $[Ru(triphos)(MeCN)_3](OTf)_2$ system, **VI**, achieves full conversion in an hour, at a catalyst loading of 12.9 μmol (FA:cat. = 100:1) at 80°C, with N,N-dimethyloctanamine as an additive, albeit with a low TON and TOF of 1000 and 100 h^{-1}, respectively [31]. The (PNP)Ir(III)-trihydride complex, **VII**, catalysed the dehydrogenation of FA in acidic water, with pH-dependent activity. The best activity, with a TOF_{max} of 1880 h^{-1}, was obtained at pH 2.8, with catalyst deactivation observed at lower pH (Table S5, Entry 7) [41]. A related PCP-Ni(II)-hydride, **VIII**, dehydrogenated FA with TONs of 626, with triethylamine as an additive, in propylene carbonate at 80°C (Table S5, Entry 8). [42] The Fe(II) tetrafluoroborate complex bearing a P_4-tetradentate ligand tetraphos, **IX**, was found to dehydrogenate FA under base-free conditions in propylene carbonate at 60°C (Table S5, Entry 9) [43]. TONs of 6061 were obtained after 6 h of reaction, with $TOF_{initial}$ of 1737 h^{-1}. As a final case in point, the $[BrMn(L)(CO)_3]$ complex, **X** (L = 2-(4,5-dihydro-1*H*-imidazol-2-yl)pyridine), reported by Beller, could dehydrogenate FA under continuous-flow conditions, with a TON of 5476 after 45 h and TOF up to 192 h^{-1} after 3 h [35]. In the context of our comparative analysis, our current system distinguishes itself with low additive requirements, i.e., an equimolar amount of catalyst and additive, catalyst durability under catalytic conditions, recyclability and full substrate conversion in a short timeframe (20 min) under optimised conditions. The ongoing quest for an efficient FADH catalyst system that aligns with all industrial requirements underscores the importance of our new system, contributing valuable insights to the design and understanding of future FADH catalyst systems.

3 | Conclusions

Complexes **C1**–**C8** were screened for FADH catalysis and were all found to be active upon activation with HCOONa in DMF at 80°C. Compound **C6** was found to be the best performing among the series and was used to optimise the reaction parameters. Different alkali metal formate additives, namely, Li, Na and K formates, were screened to determine the best performing among the group. Interestingly, under the same reaction conditions, HCOOK performed slightly better than HCOONa and HCOOLi, respectively, contrary to a trend previously reported. Our observation was attributed to the relative ease with which HCOOK reacts with the precatalyst to generate the hydride species based on the HSAB principle. The dependence of temperature on FADH was evaluated with a range of temperatures from 60°C to 100°C investigated, and the thermodynamic activation parameters were determined from Arrhenius and Eyring plots. The highly negative entropy of activation points to an associative rate-determining step. The dependence of the catalyst concentration on the rate of FADH was investigated and revealed a first-order rate dependence on the concentration of complex **C6**. An approximate half-order in [FA] was found experimentally, which allowed us to postulate a dihydrogen formation step involving hydrated protons as the hydrogen source. Remarkably, **C6** proved to be robust at 100°C, resulting in approximately 98% substrate conversion with a total TON of about 7892 and TOF close to 300 h^{-1} after 35 h of reaction. NMR studies revealed the long-term solution stability of **C6** and reduced thermal stability under non-catalytic conditions. Importantly, we obtained evidence for the ligand non-innocence of the pyridyl-formamidine ligand during Ru(II) monohydride formation, which can be exploited in rational catalyst design. Current efforts in our research group are geared toward expanding the catalytic utility of **C1–C8**.

4 | Experimental Section

4.1 | Materials and Methods

All reagents for the synthesis of the ligands and complexes were acquired from Sigma-Aldrich/Merck and used as received. All moisture- and air-sensitive reactions were performed using standard Schlenk techniques. The solvents were distilled under a nitrogen atmosphere using Na metal and benzophenone for diethyl ether and CaH_2 for dichloromethane as drying agents. FTIR analysis was done on a Bruker Alpha-P spectrometer fitted with an attenuated total reflectance (ATR) accessory and recorded as neat samples from 400 to 4000 cm^{-1}. ^1H and ^{13}C NMR spectra were recorded on a Bruker Avance III equipped with a direct observation two-channel broadband probe at 400, 500 and 600 MHz (^1H) and 150 MHz (^{13}C), respectively. Bruker Topspin 3.6.5 software was employed to operate the spectrometer and process the data. High-resolution ESI-MS characterisation was conducted on a Bruker microTOF-QII mass spectrometer recorded in the

positive ion mode. Bruker Compass 1.3 SR1 PL 3 software was employed to operate the spectrometer and process the data. EA was done with a Perkin Elmer 2400 elemental analyser with helium as the carrier gas.

4.2 | General Procedure for the Synthesis of the Ligands

Ligands **L1–L8** were synthesised as previously reported by our group [18]. The specific conditions and work-up are described in the Supporting Information.

4.3 | General Procedure for the Synthesis of the Complexes

To a stirring methanol solution of the dichloro(*p*-cymene)ruthenium(II) dimer is added a MeOH solution of the required ligand. The mixture is then allowed to stir overnight at room temperature under argon. At the end of the reaction, the solvent is reduced under vacuum and the product precipitated with diethyl ether. The supernatant is decanted, and the product is washed with diethyl ether and dried in vacuo to afford an orange powder.

4.3.1 | [RuCl(*p*-cymene)(L1)]Cl (C1)

Complex **C1** was prepared as described in the general procedure using **L1** (0.5 mmol; 106 mg) and $[Ru(p\text{-cymene})Cl_2]_2$ (0.25 mmol; 153 mg) in 10 mL methanol. Yield: 200 mg (78%). FTIR (ATR, $\tilde{\nu}$ cm^{-1}) 3023 (w) ν(N–H), 1648 (s) $\nu(C{=}N)_{imine}$, 15xx (s) $\nu(C{=}N)_{py}$. ^{1}H-NMR (600 MHz, $CDCl_3$, ppm) δ 13.30 (s, N–*H*, 1H), 8.84–8.79 (m, *H*C=N_{imine}, 1H), 7.79–7.72 (m, C*H*$_{py}$, 3H), 7.53 (d, J = 8.3 Hz, C*H*$_{py}$, 2H), 7.16 (d, J = 8.2 Hz, C*H*$_{arom}$, 2H), 7.06 (td, J = 6.7, 1.7 Hz, C*H*$_{arom}$, 1H), 5.40 (d, J = 6.1 Hz, *p*-cymene-C*H*, 1H), 5.30 (d, J = 6.0 Hz, *p*-cymene-C*H*, 1H), 5.07 (d, J = 6.1 Hz, *p*-cymene-C*H*, 1H), 4.59 (d, J = 6.0 Hz, *p*-cymene-C*H*, 1H), 2.42 (dt, J = 13.8, 6.9 Hz, *p*-cymene-C*H* $(CH_3)_2$, 1H), 2.36 (s, -C*H*$_3$, 3H), 2.00 (s, *p*-cymene-C*H*$_3$, 3H), 1.12 (d, J = 6.9 Hz, *p*-cymene-C*H*$_3$, 3H), 0.93 (d, J = 6.9 Hz, *p*-cymene-C*H*$_3$, 3H). ^{13}C-NMR (151 MHz, $CDCl_3$, ppm) δ 155.6 (*C*=N_{imine}), 151.7 (s, *C*=N_{py}), 149.9 (-N–C_{arom}), 148.8 (H*C*–N_{py}), 140.1 (*C*H$_{py}$), 137.5 (-C $(CH_3)_{arom}$), 129.9 (*C*H$_{py}$), 123.7 (*C*H$_{py}$), 120.4 (*C*H$_{arom}$), 115.8 (*C*H$_{arom}$), 105.4 (*C*H$_{arom}$), 100.4 (*C*H$_{arom}$), 86.1 (*p*-cymene-*C*H), 85.9 (*p*-cymene-*C*H), 85.1 (*p*-cymene-*C*H), 84.2 (*p*-cymene-*C*H), 30.8 (*p*-cymene-*C*H $(CH_3)_2$), 22.2 (-*C*H$_3$), 22.0 (*p*-cymene-*C*H$_3$), 21.1 (*p*-cymene-*C*H$_3$), 18.6 (*p*-cymene-*C*H$_3$). EA calculated for $C_{23}H_{27}Cl_2N_3Ru$ (found): C 53.39 (53.10), H 5.62 (5.46), N 8.46 (8.16). HRMS (ESI + mode, m/z): Calculated for $[M]^+$ 482.0100, found 482.0817.

4.3.2 | [RuCl(*p*-cymene)(L2)]Cl (C2)

Complex **C2** was prepared as described in the general procedure using **L2** (0.50 mmol; 114 mg) and $[Ru(p\text{-cymene})Cl_2]_2$ (0.25 mmol; 153 mg) in 10 mL methanol. Yield: 230 mg (89%). FTIR (ATR, $\tilde{\nu}$ cm^{-1}) 3032 (w) ν (N–H), 1645 $\nu(C{=}N)_{imine}$, $\nu(C{=}N)_{py}$. ^{1}H-NMR (600 MHz, $CDCl_3$, ppm) δ 13.32 (s, N–*H*, 1H), 8.81 (d, *J* = 5.5 Hz, *H*C=N_{imine}, 1H), 7.84–7.70 (m, C*H*$_{py}$ 3H), 7.61 (d, *J* = 8.6 Hz, C*H*$_{py}$, 2H), 7.06 (t, *J* = 6.3 Hz, C*H*$_{arom}$, 1H), 6.87 (d, *J* = 8.6 Hz, C*H*$_{arom}$, 2H), 5.42 (d, *J* = 5.6 Hz, *p*-cymene-C*H*, 1H), 5.33 (d, *J* = 5.8 Hz, *p*-cymene-C*H*, 1H), 5.07 (d, *J* = 5.7 Hz, *p*-cymene-C*H*, 1H), 4.62 (d, *J* = 5.9 Hz, *p*-cymene-C*H*, 1H), 3.82 (s, O–C*H*$_3$, 3H), 2.43 (dt, *J* = 13.7, 6.9 Hz, *p*-cymene-C*H* $(CH_3)_2$, 1H), 2.00 (s, *p*-cymene-C*H*$_3$, 3H), 1.14 (d, *J* = 6.9 Hz, *p*-cymene-C*H*$_3$, 3H), 0.94 (d, *J* = 6.9 Hz, *p*-cymene-C*H*$_3$, 3H). ^{13}C-NMR (151 MHz, $CDCl_3$, ppm) δ 158.7 (-*C* (OCH_3)), 155.6 (*C*=N_{im}), 150.1 (*C*=N_{py}), 148.7 (-N–C_{arom}), 147.5 (H*C*–N_{py}), 140.1 (*C*H$_{py}$), 124.9 (*C*H$_{py}$), 120.3 (*C*H$_{py}$), 115.9 (*C*H$_{arom}$), 114.3 (*C*H$_{arom}$), 105.5 (*C*H$_{arom}$), 100.3 (*p*-cymene-*C*H), 85.9 (*p*-cymene-*C*H), 85.2 (*p*-cymene-*C*H), 84.3 (*p*-cymene-*C*H), 55.7 (O–*C*H$_3$), 30.9 (*p*-cymene-*C*H $(CH_3)_2$), 22.3 (*p*-cymene-*C*H$_3$), 22.1 (*p*-cymene-*C*H$_3$), 18.6 (*p*-cymene-*C*H$_3$). EA calculated for $C_{23}H_{27}Cl_2N_3ORu{\cdot}CH_3OH{\cdot}H_2O$ (found): C 49.40 (49.33), H 5.70 (5.48), N 7.20 (7.50). HRMS (ESI + mode, m/z): Calculated for $[M]^+$ 498.0100, found 498.0846.

4.3.3 | [RuCl(*p*-cymene)(L3)]Cl (C3)

Complex **C3** was synthesised following the general procedure, using **L5** (0.5 mmol; 121 mg) and $[Ru(p\text{-cymene})Cl_2]_2$ (0.25 mmol; 153 mg) in 10 mL methanol. Yield: 217 mg (79%). FTIR (ATR, $\tilde{\nu}$ cm^{-1}) 3052 (w) ν (N–H), 1642 (s) $\nu(C{=}N)_{imine}$, (s) $\nu(C{=}N)_{py}$. ^{1}H-NMR (600 MHz, $CDCl_3$, ppm) δ 8.10 (d, *J* = 5.8 Hz, *H*C=N_{imine}, 1H), 7.57 (t, *J* = 5.9 Hz, C*H*$_{py}$, 2H), 7.41 (dd, *J* = 9.4, 2.3 Hz, C*H*$_{py}$, 2H), 7.15 (d, *J* = 3.7 Hz, C*H*$_{arom}$, 2H), 6.46 (td, *J* = 5.6, 3.4 Hz, *p*-cymene-C*H*, 1H), 4.96 (d, *J* = 6.0 Hz, *p*-cymene-C*H*, 1H), 4.80 (d, *J* = 6.0 Hz, *p*-cymene-C*H*, 1H), 4.35 (d, *J* = 6.0 Hz, *p*-cymene-C*H*, 1H), 4.06 (d, *J* = 6.0 Hz, *p*-cymene-C*H*, 1H), 1.75 (dt, *J* = 13.8, 6.9 Hz, *p*-cymene-C*H* $(CH_3)_2$, 1H), 1.27 (s, *p*-cymene-C*H*$_3$, 3H), 0.44 (d, *J* = 7.0 Hz, *p*-cymene-C*H*$_3$, 3H), 0.19 (d, *J* = 6.9 Hz, *p*-cymene-C*H*$_3$, 3H). ^{13}C-NMR (151 MHz, $CDCl_3$, ppm) δ 157.6 (-*C* (NO_2)), 150.7 (*C*=N_{py}), 147.2 (H*C*–N_{py}), 139.9 (*C*H$_{py}$), 124.6 (*C*H$_{arom}$), 124.1 (*C*H$_{arom}$), 120.4 (*C*H$_{arom}$), 114.1 (*p*-cymene-*C*H), 85.6 (*p*-cymene-*C*H), 84.5 (*p*-cymene-*C*H), 82.9 (*p*-cymene-*C*H), 29.9 (*p*-cymene-*C*H $(CH_3)_2$), 21.4 (*p*-cymene-*C*H$_3$), 20.9 (*p*-cymene-*C*H$_3$), 17.5 (*p*-cymene-*C*H$_3$). EA calculated for $C_{22}H_{24}Cl_2N_4O_2Ru{\cdot}CH_2Cl_2$ (found): C 43.62 (43.37), H 4.64 (4.36), N 8.85 (8.61). HRMS (ESI + mode, m/z): Calculated for $[M]^+$ 512.9800, found 513.0552.

4.3.4 | [RuCl(*p*-cymene)(L4)]Cl (C4)

Complex **C4** was prepared as outlined in the general procedure, using **L3** (0.338 mmol; 76 mg) and $[Ru(p\text{-cymene})Cl_2]_2$ (0.169 mmol; 103 mg) in 10 mL methanol. Yield: 153 mg (85%). FTIR (ATR, $\tilde{\nu}$ cm^{-1}) 3024 (w) ν (N–H), 1646 (s) $\nu(C{=}N)_{imine}$, (s) $\nu(C{=}N)_{py}$. ^{1}H-NMR (600 MHz, $CDCl_3$, ppm) δ 13.31 (s, N–*H*, 1H), 8.62 (d, J = 6.1 Hz, *H*C=N_{imine}, 1H), 7.77 (s, C*H*$_{py}$, 1H), 7.57–7.51 (m, C*H*$_{py}$, 3H), 7.16 (d, J = 8.0 Hz, C*H*$_{arom}$, 2H), 6.88 (d, J = 5.9 Hz, C*H*$_{arom}$, 1H), 5.33 (d, J = 6.0 Hz, *p*-cymene-C*H*, 1H), 5.27 (d, J = 5.9 Hz, *p*-cymene-C*H*, 1H), 5.04 (d, J = 5.9 Hz, *p*-cymene-C*H*, 1H), 4.56 (d, J = 5.9 Hz, *p*-cymene-C*H*, 1H), 2.44 (dt, J = 13.8, 6.9 Hz, *p*-cymene-C*H* $(CH_3)_2$, 1H), 2.37 (d, J = 3.6 Hz, -C*H*$_3$, 6H), 2.02 (s, *p*-cymene-C*H*$_3$, 3H), 1.14 (d, J = 6.9 Hz, *p*-cymene-C*H*$_3$, 3H), 0.95 (d, J = 6.9 Hz, *p*-cymene-C*H*$_3$, 3H). ^{13}C-NMR (151 MHz, $CDCl_3$, ppm) δ 154.7 (*C*=N_{imine}), 152.7 (*C*=N_{py}), 151.8 (-N–C_{arom}), 150.3 (H*C*–N_{py}), 148.3 (-N–C_{arom}), 137.4 (*C*H$_{py}$), 129.9 (*C*H$_{py}$), 123.7 (*C*H$_{arom}$), 122.1 (-*C* $(CH_3)_{arom}$), 115.8 (*C*H$_{arom}$), 105.3

(CH_{arom}), 100.3 (*p*-cymene-*C*H), 85.9 (*p*-cymene-*C*H), 84.9 (*p*-cymene-*C*H), 84.1 (*p*-cymene-*C*H), 30.9 (*p*-cymene-*C*H (CH_3)$_2$), 22.3 (-*C*H_3), 22.1 (*p*-cymene-CH_3), 21.1 (*p*-cymene-*C*H_3), 18.6 (*p*-cymene-*C*H_3). EA calculated for $C_{24}H_{29}Cl_2N_3Ru$ (found): C 54.24 (53.96), H 5.50 (5.53), N 7.91 (8.12). HRMS (ESI + mode, m/z): Calculated for $[M]^+$ 496.0400, found 496.1124.

4.3.5 | [RuCl(*p*-cymene)(L5)]Cl (C5)

Complex **C5** was prepared as outlined in the general procedure, using **L4** (0.50 mmol; 121 mg) and $[Ru(p\text{-cymene})Cl_2]_2$ (0.25 mmol; 153 mg) in 10 mL methanol. Yield: 249 mg (91%). FTIR (ATR, $\tilde{\nu}$ cm^{-1}) 3033 (w) ν (N–H), 1648 (s) ν(C=N)$_{imine}$, (s) ν(C=N)$_{py}$. ^{1}H-NMR (600 MHz, $CDCl_3$, ppm) δ 13.19 (s, N–*H*, 1H), 8.62 (d, *J* = 5.3 Hz, *H*C=N$_{imine}$, 1H), 7.78 (s, 1H), 7.62–7.50 (m, C*H*$_{py}$, 3H), 6.86 (d, *J* = 8.1 Hz, C*H*$_{arom}$, 3H), 5.43–5.23 (m, *p*-cymene-C*H*, 2H), 5.04 (s, *p*-cymene-C*H*, 1H), 4.58 (d, *J* = 5.5 Hz, *p*-cymene-C*H*, 1H), 3.82 (s, O–C*H*$_3$, 3H), 2.43 (dd, *J* = 13.3, 6.6 Hz, *p*-cymene-C*H* (CH_3)$_2$, 1H), 2.36 (s, -C*H*$_3$, 3H), 2.01 (s, *p*-cymene-C*H*$_3$, 3H), 1.13 (d, *J* = 6.8 Hz, *p*-cymene-C*H*$_3$, 3H), 0.95 (d, *J* = 6.8 Hz, *p*-cymene-C*H*$_3$, 3H). ^{13}C-NMR (151 MHz, $CDCl_3$, ppm) δ 158.7 (-C (OCH$_3$)), 154.7 (*C*=N$_{imine}$), 152.6 (*C*=N$_{py}$), 150.3 (-N–C$_{arom}$), 148.3 (H*C*–N$_{py}$), 147.6 (*C*H$_{py}$), 125.0 (-*C* (CH_3)), 122.1 (*C*H$_{py}$), 115.8 (*C*H$_{py}$), 114.3 (CH_{arom}), 105.3 (CH_{arom}), 100.3 (*p*-cymene-CH), 86.1 (*p*-cymene-*C*H), 85.9 (*p*-cymene-*C*H), 85.1 (*p*-cymene-*C*H), 84.2 (*p*-cymene-*C*H), 55.7 (O–*C*H$_3$), 30.9 (*p*-cymene-*C*H (CH_3)$_2$), 22.3 (-*C*H_3), 22.1 (*p*-cymene-*C*H_3), 21.1 (*p*-cymene-*C*H_3), 18.6 (*p*-cymene-CH_3). EA calculated for $C_{24}H_{29}Cl_2N_3ORu{\cdot}CH_3OH{\cdot}H_2O$ (found): C 50.52 (50.82), H 5.90 (6.20), N 7.03 (7.28). HRMS (ESI + mode, m/z): Calculated for $[M]^+$ 512.0400, found 512.1033.

4.3.6 | [RuCl(*p*-cymene)(L6]Cl (C6)

Complex **C6** was prepared as described in the general procedure, using **L6** (0.50 mmol; 128 mg) and $[Ru(p\text{-cymene})Cl_2]_2$ (0.25 mmol; 153 mg) in 10 mL methanol. At the end of the reaction, the product precipitated out of the solution and the solvent was decanted. The product was washed with diethyl ether and dried in vacuo to afford yellow powder. Yield: 262 mg (93%). FTIR (ATR, $\tilde{\nu}$ cm^{-1}) 3032 ν (N–H), 1629 (s) ν(C=N)$_{imine}$, (s) ν(C=N)$_{py}$. ^{1}H-NMR (600 MHz, $CDCl_3$, ppm) δ 8.62 (d, *J* = 6.1 Hz, N–*H*, 1H), 8.29 (d, *J* = 8.9 Hz, *H*C=N$_{imine}$; C*H*$_{py}$ 2H), 8.08 (d, *J* = 8.9 Hz, C*H*$_{py}$, 2H), 7.95 (s, C*H*$_{py}$, 1H), 7.65 (s, C*H*$_{arom}$, 1H), 6.99 (d, *J* = 5.1 Hz, C*H*$_{arom}$, 1H), 5.56 (d, *J* = 6.0 Hz, *p*-cymene-C*H*, 1H), 5.44 (d, *J* = 6.0 Hz, *p*-cymene-C*H*, 1H), 5.04 (d, *J* = 6.0 Hz, *p*-cymene-C*H*, 1H), 4.73 (d, *J* = 6.0 Hz, *p*-cymene-C*H*, 1H), 2.52–2.43 (m, -CH_3; *p*-cymene-C*H* (CH_3)$_2$, 4H), 2.01 (s, *p*-cymene-C*H*$_3$, 3H), 1.17 (d, *J* = 6.9 Hz, *p*-cymene-C*H*$_3$, 3H), 0.94 (d, *J* = 6.9 Hz, *p*-cymene-C*H*$_3$, 3H). ^{13}C-NMR (151 MHz, $CDCl_3$, ppm) δ 158.5 (-*C* (NO_2)), 154.7 (*C*=N$_{imine}$), 153.4 (*C*=N$_{py}$), 152.1 (-N–C$_{arom}$), 148.2 (H*C*–N$_{py}$), 146.5 (*C*H$_{py}$), 125.4 (-*C* (CH_3)), 125.1 (*C*H$_{py}$), 122.9 (*C*H$_{py}$), 116.2 (*C*H$_{arom}$), 106.5 (*C*H$_{arom}$), 99.9 (*p*-cymene-*C*H), 85.8 (*p*-cymene-*C*H), 85.1 (*p*-cymene-*C*H), 83.8 (*p*-cymene-*C*H), 30.9 (*p*-cymene-*C*H (CH_3)$_2$), 22.4 (-*C*H_3), 21.9 (*p*-cymene-*C*H_3), 21.2 (*p*-cymene-*C*H_3), 18.6 (*p*-cymene-CH_3). EA calculated for $C_{23}H_{26}Cl_2N_4O_2Ru{\cdot}H_2O$ (found): C 47.59 (47.51), H 4.86 (5.11), N 9.65 (9.95). HRMS (ESI + mode, m/z): Calculated for $[M]^+$ 527.0100, found 527.0729.

4.3.7 | [RuCl(*p*-cymene)(L7)]Cl (C7)

Complex **C7** was prepared as outlined in the general procedure using **L7** (0.50 mmol; 122 mg) and $[Ru(p\text{-cymene})Cl_2]_2$ (0.25 mmol; 153 mg) in 10 mL methanol. Yield: 181 mg (65%). FTIR (ATR, $\tilde{\nu}$ cm^{-1}) 3029 (w) ν (N–H), 1645 (s) ν(C=N)$_{imine}$, (s) ν(C=N)$_{py}$. ^{1}H-NMR (600 MHz, $CDCl_3$, ppm) δ 13.59 (s, N–*H*, 1H), 8.70 (d, *J* = 6.5 Hz, *H*C=N$_{imine}$, 1H), 7.84 (d, *J* = 21.3 Hz, C*H*$_{py}$, 2H), 7.54 (d, *J* = 8.0 Hz, C*H*$_{py}$, 2H), 7.19 (d, *J* = 8.0 Hz, C*H*$_{arom}$, 2H), 7.07 (d, *J* = 5.2 Hz, C*H*$_{arom}$, 1H), 5.40 (d, *J* = 6.0 Hz, *p*-cymene-C*H*, 1H), 5.33 (d, *J* = 5.9 Hz, *p*-cymene-C*H*, 1H), 5.06 (d, *J* = 6.0 Hz, *p*-cymene-C*H*, 1H), 4.62 (d, *J* = 5.9 Hz, *p*-cymene-C*H*, 1H), 2.47 (dt, *J* = 13.8, 6.8 Hz, *p*-cymene-C*H* (CH_3)$_2$, 1H), 2.38 (s, *p*-cymene-C*H*$_3$, 3H), 2.04 (s, -C*H*$_3$, 3H), 1.17 (d, *J* = 6.9 Hz, *p*-cymene-C*H*$_3$, 4H), 0.98 (d, *J* = 6.9 Hz, *p*-cymene-C*H*$_3$, 3H). ^{13}C-NMR (151 MHz, $CDCl_3$, ppm) δ 155.7 (*C*=N$_{imine}$), 151.5 (*C*=N$_{py}$), 150.4 (-N–C$_{arom}$), 149.5 (H*C*–N$_{py}$), 148.3 (*C*H$_{py}$), 137.8 (*C*H$_{py}$), 129.9 (*C*H$_{py}$), 123.7 (*C*H$_{arom}$), 121.2 (*C*H$_{arom}$), 115.4 (*C*H$_{arom}$), 105.8 (*C*H$_{arom}$), 100.5 (*p*-cymene-CH), 85.8 (*p*-cymene-CH), 85.3 (*p*-cymene-*C*H), 84.4 (*p*-cymene-*C*H), 30.9 (*p*-cymene-*C*H (CH_3)$_2$), 22.2 (-*C*H_3; *p*-cymene-*C*H_3), 21.1 (*p*-cymene-*C*H_3), 18.7 (*p*-cymene-*C*H_3). EA calculated for $C_{23}H_{26}Cl_3N_3Ru{\cdot}H_2O$ (found): C 48.47 (48.47), H 4.95 (4.95), N 7.37 (7.61). HRMS (ESI + mode, m/z): Calculated for $[M + CH_2Cl_2]^+$ 601.3800, found 601.1250.

4.3.8 | [RuCl(*p*-cymene)(L8)]l (C8)

Complex **C8** was prepared as outlined in the general procedure, using **L8** (0.5 mmol; 131 mg) and $[Ru(p\text{-cymene})Cl_2]_2$ (0.25 mmol; 153 mg) in 10 mL methanol. Yield: 240 mg (84%). FTIR (ATR, $\tilde{\nu}$ cm^{-1}) 3057 (w) ν (N–H), 1640 (s) ν(C=N)$_{imine}$, (s) ν(C=N)$_{py}$. ^{1}H-NMR (600 MHz, $CDCl_3$, ppm) δ 13.57 (s, N–*H*, 1H), 8.77 (d, *J* = 5.9 Hz, *H*C=N$_{imine}$, 1H), 7.80 (d, *J* = 30.4 Hz, C*H*$_{py}$, 2H), 7.60 (d, *J* = 8.5 Hz, C*H*$_{py}$, 2H), 7.08 (d, *J* = 5.6 Hz, C*H*$_{arom}$, 1H), 6.88 (d, *J* = 8.4 Hz, C*H*$_{arom}$, 2H), 5.48 (d, *J* = 4.4 Hz, *p*-cymene-C*H*, 1H), 5.35 (d, *J* = 5.7 Hz, *p*-cymene-C*H*, 1H), 5.10 (d, *J* = 4.6 Hz, *p*-cymene-C*H*, 1H), 4.64 (d, *J* = 5.7 Hz, *p*-cymene-C*H*, 1H), 3.83 (s, -OC*H*$_3$, 3H), 2.46 (dt, *J* = 13.6, 6.8 Hz, *p*-cymene-C*H* (CH_3)$_2$, 1H), 2.02 (s, *p*-cymene-C*H*$_3$, 3H), 1.15 (d, *J* = 6.9 Hz, *p*-cymene-C*H*$_3$, 3H), 0.97 (d, *J* = 6.8 Hz, *p*-cymene-C*H*$_3$, 3H). ^{13}C-NMR (151 MHz, $CDCl_3$, ppm) δ 158.9 (-C (OCH$_3$)), 156.1 (*C*=N$_{imine}$), 150.2 (*C*=N$_{py}$), 149.3 (-N–*C*$_{arom}$), 148.2 (H*C*–N$_{py}$), 147.4 (*C*H$_{py}$), 124.9 (*C*H$_{py}$), 121.1 (*C*H$_{py}$), 115.3 (*C*H$_{arom}$), 114.4 (*C*H$_{arom}$), 105.7 (*C*H$_{arom}$), 100.5 (*p*-cymene-*C*H), 85.9 (*p*-cymene-*C*H), 85.4 (*p*-cymene-*C*H), 84.4 (*p*-cymene-*C*H), 55.8 (-O*C*H$_3$), 30.9 (*p*-cymene-*C*H (CH_3)$_2$), 22.2 (*p*-cymene-*C*H_3), 18.7 (*p*-cymene-*C*H_3). EA calculated for $C_{23}H_{26}Cl_3N_3ORu$ (found): C 48.64 (48.82), H 4.61 (4.61), N 7.40 (7.58). HRMS (ESI + mode, m/z): Calculated for $[M]^+$ 532.0530, found 532.0485.

4.4 | General Procedure for the Dehydrogenation of FA

The procedure is modified from a previously reported method [16]. The required amount of alkali metal formate additive was weighed into a 50 mL two-neck round-bottomed flask and kept under nitrogen. A stock solution of the precatalyst was prepared in DMF by weighing the required amount of the complex into a

volumetric flask and topping up the solvent to the mark. From the stock solution, 1 mL was added to the round-bottomed flask and the atmosphere exchanged for nitrogen. The solution was stirred for 5 min at room temperature. Then, FA was added, and the mixture was stirred for an additional minute. The mixture was then heated at the desired temperature using a pre-heated oil bath equipped with a thermometer, and the gas generated was monitored using a BlueSens BlueVcount gas measuring device operating at ambient conditions.

4.5 | Procedure for Continuous FA Addition Reaction

A 0.075 M stock solution of HCOOK was prepared in methanol. From the stock solution, 1 mL was added to a two-neck round-bottomed flask, and the volatiles were removed under vacuum. After all the volatiles were removed, 1 mL of stock solution of the catalyst (0.05 M) in DMF was added to the flask via a septum, and the contents were stirred for 5 min at room temperature. Then 0.2 mL FA was added, and the mixture was stirred for an additional minute, after which the flask was placed in a preheated oil bath at 100°C, and an NE-300 Just Infusion syringe pump was used to inject FA via a long tube at a rate of 0.01 mL/min after the immersion of the round-bottomed flask in the oil bath.

4.6 | Analysis of Gas Samples by GC-TCD

The produced gas mixture from the FADH reactions was analysed using an online SRI 8610C gas chromatograph (SRI Instruments, Torrance, CA, USA) fitted with a HayeSepD column and two molecular sieve 13X columns. The instrument was also fitted with two thermal conductivity detectors.

4.7 | X-Ray Crystal Structure Determination

Data for single-crystal X-ray diffraction were collected using a Bruker Apex DUO diffractometer equipped with a CCD area detector [44] utilising graphite-monochromated Mo-Kα radiation (λ = 0.71073 Å). Data collection, reduction and refinement were conducted with the SMART and SAINT software packages [45, 46]. Absorption corrections [47] and other systematic errors were addressed using SADABS [48]. The structures were solved via direct methods and refined using full-matrix least-squares on F^2 with SHELXS-13 and SHELXL-16 [49, 50], operated within the X-Seed graphical user interface [44, 51]. Non-hydrogen atoms were refined anisotropically, while hydrogen atoms were placed in calculated positions using riding models. High-resolution molecular diagrams were generated with POV-Ray [52]. Crystallographic data are deposited at the CCDC under the accession numbers 2251445 (**C9**), 2251446 (**C8**), 2382057 (**C2**), 2382058 (**C1**), 2251447 (**C10**) and 2251448 (**C11**).

Author Contributions

Juliana Mana Edor: investigation, writing – original draft. **M. Cassiem Joseph:** writing – original draft, investigation. **Johan H. L. Jordaan:** writing – review and editing, formal analysis, supervision. **Hermanus C. M. Vosloo:** writing – review and editing, supervision, formal analysis. **Andrew J. Swarts:** conceptualization, funding acquisition, writing – review and editing, project administration, supervision, resources.

Acknowledgements

Financial support from the Schlumberger Foundation's Faculty for the Future Program, the Organisation for Women in Science for the Developing World (OWSD), and the Swedish International Development Cooperation Agency (SIDA) is duly acknowledged. AJS acknowledges funding support from the National Research Foundation (ZA), with grant numbers 137758 and 127291.

Conflicts of Interest

The authors declare no conflicts of interest.

Data Availability Statement

The data that support the findings of this study are available in the Supporting Information of this article.

References

1. (a) D. Huang, P. Zhao, and D. Astruc, "Catalysis by 1,2,3-Triazole- and Related Transition-Metal Complexes," *Coordination Chemistry Reviews* 272 (2014): 145–165. (b) M. C. Joseph, A. J. Swarts, and S. F. Mapolie, "Transition Metal Complexes of Click-Derived 1,2,3-Triazoles as Catalysts in Various Transformations: An Overview and Recent Developments," *Coordination Chemistry Reviews* 493 (2023): 215317.

2. S. Günnaz, N. Özdemir, S. Dayan, O. Dayan, and B. Çetinkaya, "Synthesis of Ruthenium(II) Complexes Containing Tridentate Triamine (′N⁀N⁀N′) and Bidentate Diamine Ligands (N⁀N′): As Catalysts for Transfer Hydrogenation of Ketones," *Organometallics* 30 (2011): 4165–4173.

3. M. C. Joseph, A. J. Swarts, and S. F. Mapolie, "Cationic Half-Sandwich Ruthenium(II) Complexes Ligated by Pyridyl-Triazole Ligands: Transfer Hydrogenation and Mechanistic Studies," *Polyhedron* 212 (2022): 115579.

4. J. M. Gichumbi, H. B. Friedrich, and B. Omondi, "Synthesis and Characterization of Some New Half-Sandwich Ruthenium(II) Complexes With Bidentate N,N′-Ligands and Their Application in Alcohol Oxidation," *Inorganica Chimica Acta* 456 (2017): 55–63.

5. P. Singh and A. K. Singh, "Transfer Hydrogenation of Ketones and Catalytic Oxidation of Alcohols with Half-Sandwich Complexes of Ruthenium(II) Designed Using Benzene and Tridentate (S, N, E) Type Ligands (E = S, Se, Te)," *Organometallics* 29 (2010): 6433–6442.

6. R. H. Grubs, A. G. Wenzel, and A. K. Chatterjee, *Comprehensive Organometallic Chemistry III—Olefin Cross—Metathesis*, vol. 11, eds. D. M. P. Mingos and R. H. Crabtree (Amsterdam: Elsevier, 2007), 179.

7. T. T. Tole, J. H. L. Jordaan, and H. C. M. Vosloo, "Catalysis of Linear Alkene Metathesis by Grubbs-Type Ruthenium Alkylidene Complexes Containing Hemilabile α,α-Diphenyl-(monosubstituted-pyridin-2-yl) methanolato Ligands," *Beilstein Journal of Organic Chemistry* 15 (2019): 194–209.

8. E. Pump, A. Poater, N. Bahri-Laleh, et al., "Regio, Stereo and Chemoselectivity of 2nd Generation Grubbs Ruthenium-Catalyzed Olefin Metathesis," *Catalysis Today* 388 (2022): 394–402.

9. I. Dragutan, V. Dragutan, and A. Demonceau, "Editorial of Special Issue Ruthenium Complex: The Expanding Chemistry of the Ruthenium Complexes," *Molecules* 20 (2015): 17244–17274.

10. E. Ispir and A. Aktas, "KSU Mühendislik Bilim," Derg., 19 (2016): 37.

11. Y. Harada, T. Ikeue, Y. Ide, et al., "Synthesis, Structures, and Properties of Lantern-Type Dinuclear Ruthenium(II,III) Complexes *cis*-[Ru_2{3,5-$(CF_3)_2$-pf}$_2(O_2CMe)_2Cl$] and [Ru_2{3,5-$(CF_3)_2$-pf}$_3(O_2CMe)Cl$], 3,5-$(CF_3)_2$-pf$^-$ =*N*,*N*′-bis[3,5-bis(trifluoromethyl)phenyl]formamidinate Anion," *Inorganica Chimica Acta* 424 (2015): 186–193.

12. M. C. Joseph, I. A. Kotzé, N. J. Nnaji, A. J. Swarts, and S. F. Mapolie, "Structural Investigation of the Anion Effect in Ruthenium(II) Arene Complexes Bearing Pyridyl-Triazole Ligands: Implications for Transfer Hydrogenation Catalysis," *Organometallics* 41 (2022): 3546–3556.

13. M. Cortijo, R. González-Prieto, S. Herrero, J. L. Priego, and R. Jiménez-Aparicio, "The Use of Amidinate Ligands in Paddlewheel Diruthenium Chemistry," *Coordination Chemistry Reviews* 400 (2019): 213040.

14. C. R. K. Rao and D. C. Trivedi, "Chemical and Electrochemical Depositions of Platinum Group Metals and Their Applications," *Coordination Chemistry Reviews* 249 (2005): 613–631.

15. P. Kumar, R. K. Gupta, and D. S. Pandey, "Half-Sandwich Arene Ruthenium Complexes: Synthetic Strategies and Relevance in Catalysis," *Chemical Society Reviews* 43 (2014): 707–733.

16. N. Onishi, R. Kanega, H. Kawanami, and Y. Himeda, "Recent Progress in Homogeneous Catalytic Dehydrogenation of Formic Acid," *Molecules* 27 (2022): 455.

17. C. Guan, Y. Pan, T. Zhang, M. J. Ajitha, and K.-W. Huang, "An Update on Formic Acid Dehydrogenation by Homogeneous Catalysis," *Chemistry, An Asian Journal* 15 (2020): 937–946.

18. J. M. Edor, M. C. Joseph, J. H. L. Jordaan, H. C. M. Vosloo, and A. J. Swarts, "Synthesis, Characterisation, and Coordination Behaviour of Novel Pyridyl-Formamidine Based Mn(I), Cu(II), Zn(II), and Pd(II) Complexes," *European Journal of Inorganic Chemistry* 28 (2025): e202400585.

19. T. S. Ramos, D. M. Luz, R. D. Nascimento, et al., "Ruthenium-Cymene Containing Pyridine-Derived Aldiimine Ligands: Synthesis, Characterization and Application in the Transfer Hydrogenation of Aryl Ketones and Kinetics Studies," *Journal of Organometallic Chemistry* 892 (2019): 51–65.

20. R. Ruzziconi, G. Bellachioma, G. Ciancaleoni, et al., "Cationic Half-Sandwich Quinolinophaneoxazoline-Based (η6-p-cymene)ruthenium(ii) Complexes Exhibiting Different Chirality Types: Synthesis and Structural Determination by Complementary Spectroscopic Methods," *Dalton Transactions* 43 (2014): 1636–1650.

21. M. Abrahamsson, H. C. Becker, L. Hammarström, C. Bonnefous, C. Chamchoumis, and R. P. Thummel, "Six-Membered Ring Chelate Complexes of Ru(II): Structural and Photophysical Effects," *Inorganic Chemistry* 46 (2007): 10354–10364.

22. D. A. Bardwell, J. C. Jeffery, E. Schatz, E. E. M. Tilley, and M. D. Ward, "Conventional and Cyclometallated Complexes of Ruthenium(II) With Ambidentate Terdentate Ligands Displaying N3 or N2C Binding Modes," *Journal of the Chemical Society, Dalton Transactions* 5 (1995): 825–834.

23. F. A. Cotton, P. Lei, C. A. Murillo, and L. Wang, "Synthesis of Unsymmetrical Formamidines and Benzamidines: Structural Studies of Copper, Cobalt and Chromium Complexes," *Inorganica Chimica Acta* 349 (2003): 165–172.

24. R. J. Lundgren and M. Stradiotto, *Ligand Design in Metal Chemistry: Reactivity and Catalysis*, 1st ed., eds. R. J. Lundgren and M. Stradiotto (New Jersey: Wiley, 2016), 7.

25. S. Oldenhof, M. Lutz, B. De Bruin, J. I. Van Der Vlugt, and J. N. H. Reek, "Dehydrogenation of Formic Acid by Ir–bisMETAMORPhos Complexes: Experimental and Computational Insight Into the Role of a Cooperative Ligand," *Chemical Science* 6 (2015): 1027–1034.

26. C. Guan, D. D. Zhang, Y. Pan, et al., "Dehydrogenation of Formic Acid Catalyzed by a Ruthenium Complex with an N,N′-Diimine Ligand," *Inorganic Chemistry* 56 (2017): 438–445.

27. P. W. Atkins, *Shriver and Atkins' Inorganic Chemistry*, 5th ed. (New York: Oxford University Press, Oxford, 2010).

28. N. Lentz and M. Albrecht, "A Low-Coordinate Iridium Complex With a Donor-Flexible O,N-Ligand for Highly Efficient Formic Acid Dehydrogenation," *ACS Catalysis* 12 (2022): 12627–12631.

29. E. A. Bielinski, P. O. Lagaditis, Y. Zhang, et al., "Lewis Acid-Assisted Formic Acid Dehydrogenation Using a Pincer-Supported Iron Catalyst," *Journal of the American Chemical Society* 136 (2014): 10234–10237.

30. S. Kar, M. Rauch, G. Leitus, Y. Ben-David, and D. Milstein, "Highly Efficient Additive-Free Dehydrogenation of Neat Formic Acid," *Nature Catalysis* 4 (2021): 193–201.

31. I. Mellone, M. Peruzzini, L. Rosi, et al., "Formic Acid Dehydrogenation Catalysed by Ruthenium Complexes Bearing the Tripodal Ligands Triphos and NP3," *Dalton Transactions* 42 (2013): 2495–2501.

32. Z. Wang, S. M. Lu, J. Li, J. Wang, and C. Li, "Unprecedentedly High Formic Acid Dehydrogenation Activity on an Iridium Complex With an N,N′-Diimine Ligand in Water," *Chemistry—A European Journal* 21 (2015): 12592–12595.

33. A. K. Galwey and M. E. Brown, "Chapter 4 The Influence of Temperature on Reaction Rate," in *Studies in Physical and Theoretical Chemistry*, vol. 86 (Amsterdam: Elsevier, 1999), 117–138.

34. (a) S. Fukuzumi, T. Kobayashi, and T. Suenobu, "Efficient Catalytic Decomposition of Formic Acid for the Selective Generation of H_2 and H/D Exchange with a Water-Soluble Rhodium Complex in Aqueous Solution," *ChemSusChem: Chemistry & Sustainability Energy & Materials* 1 (2008): 827–834. (b) O. Manuel and I. Enrique, "Formic Acid Dehydrogenation on Au-Based Catalysts at Near-Ambient Temperatures," *Angewandte Chemie International Edition* 48 (2009): 4800–4803.

35. A. Léval, A. Agapova, C. Steinlechner, E. Alberico, H. Junge, and M. Beller, "Hydrogen Production From Formic Acid Catalyzed by a Phosphine Free Manganese Complex: Investigation and Mechanistic Insights," *Green Chemistry* 22 (2020): 913–920.

36. G. A. Filonenko, R. van Putten, E. N. Schulpen, E. J. M. Hensen, and E. A. Pidko, "Highly Efficient Reversible Hydrogenation of Carbon Dioxide to Formates Using a Ruthenium PNP-Pincer Catalyst," *ChemCatChem* 6 (2014): 1526–1530.

37. J. Real, E. Prat-Gil, M. Pagès-Barenys, A. Polo, J. F. Piniella, and Á. Álvarez-Larena, "Platinum Phosphinothiolato Hydride Complexes: Synthesis, Structure and Evaluation as Tin-Free Hydroformylation Catalysts," *Dalton Transactions* 45 (2016): 3964–3973.

38. (a) G. Amenuvor, J. Darkwa, and B. C. E. Makhubela, "Homogeneous Polymetallic Ruthenium(II)^Zinc(II) Complexes: Robust Catalysts for the Efficient Hydrogenation of Levulinic Acid to γ-Valerolactone," *Catalysis Science & Technology* 8 (2018): 2370–2380. (b) C. Fellay, N. Yan, P. J. Dyson, and G. Laurenczy, "Selective Formic Acid Decomposition for High-Pressure Hydrogen Generation: A Mechanistic Study," *Chemistry—A European Journal* 15 (2009): 3752–3760.

39. G. Kovács, G. Schubert, F. Joó, and I. Pápai, "Theoretical Investigation of Catalytic HCO_3^- Hydrogenation in Aqueous Solutions," *Catalysis Today* 115 (2006): 53–60.

40. R. Verron, E. Puig, P. Sutra, A. Igau, and C. Fischmeister, "Base-Free Reversible Hydrogen Storage Using a Tethered π-Coordinated-Phenoxy Ruthenium-Dimer Precatalyst," *ACS Catalysis* 13 (2023): 5787–5794.

41. R. Tanaka, M. Yamashita, and K. Nozaki, "Catalytic Hydrogenation of Carbon Dioxide Using Ir(III)−Pincer Complexes," *Journal of the American Chemical Society* 131 (2009): 14168–14169.

42. S. Enthaler, A. Brück, A. Kammer, H. Junge, E. Irran, and S. Gülak, "Exploring the Reactivity of Nickel Pincer Complexes in the Decomposition of Formic Acid to CO_2/H_2 and the Hydrogenation of $NaHCO_3$ to HCOONa," *ChemCatChem* 7 (2015): 65–69.

43. F. Bertini, I. Mellone, A. Ienco, M. Peruzzini, and L. Gonsalvi, "Iron(II) Complexes of the Linearrac-Tetraphos-1 Ligand as Efficient

Homogeneous Catalysts for Sodium Bicarbonate Hydrogenation and Formic Acid Dehydrogenation," *ACS Catalysis* 5 (2015): 1254–1265.

44. J. L. Atwood and L. J. Barbour, "Molecular Graphics: From Science to Art," *Crystal Growth & Design* 3 (2003): 3–8.

45. "Apex2 Data Collection Software", Bruker AXS, (2010).

46. SAINT, "Data Reduct. Software", Bruker AXS, (2003).

47. R. H. Blessing, "An Empirical Correction for Absorption Anisotropy," *Acta Crystallographica Section A* 51 (1995): 33–38.

48. "SADABS. Version 2.05", Bruker AXS, 2002.

49. G. M. Sheldrick, "SHELXT—Integrated Space-Group and Crystal-Structure Determination," *Acta Crystallographica Section C* 74 (2015): 3–8.

50. G. M. Sheldrick, "A Short History of SHELX," *Acta Crystallographica Section A: Foundations of Crystallography* 64 (2007): 112–122.

51. L. J. Barbour, "X-Seed—A Software Tool for Supramolecular Crystallography," *Journal of Supramolecular Chemistry* 1 (2001): 189–191.

52. POV-Ray, "POV-RAY. Version 3.6 Williamstown, Australia, Persistence of Vision Ray."

Supporting Information

Additional supporting information can be found online in the Supporting Information section.